RSC Advances

PAPER

View Article Online
View Journal | View Issue

Cite this: *RSC Adv.*, 2024, **14**, 2727

Phase transitions and spectral shifts: a quantum mechanical exploration of vibrational frequency in magnesium ferrite†

Tahani Saad Almutairi *

Spinel ferrites represent an integral subset of magnetic materials, with their inherent properties largely influenced by cation occupancy and spin interaction. In this study, we present an in-depth theoretical exploration of the phase transition landscape of pure magnesium-ferrite, deploying hybrid functionals and a local Gaussian basis set to scrutinize the relaxed lattice structure, relative energy, magnetic properties, electronic characteristics, and vibrational frequencies. Our investigation reveals that the ground state of magnesium-ferrite is an open-shell system with an inverse structure. This is characterized by the complete occupancy of octahedral sites by magnesium atoms, with Iron atoms dispersed between both tetrahedral and octahedral sites. We found a relative energy difference of 0.41 eV between the antiferromagnetic ground configuration and the ferro arrangement within the inverse structure. Furthermore, our research also delved into the impact of spin rearrangement and inversion (X = 0.0, 0.5 and 1) on Raman and infrared spectra. Notably, the lattice distortion from the cubic form, apparent in the optimized structure, resonates in the IR and Raman spectra, resulting in significant splitting. The frequencies calculated in this study align well with experimental values, suggesting that the literature's current assignments warrant reevaluation in light of this new data. The results presented herein can be instrumental in detecting the phase of Mg ferrites from experimental spectra, thereby paving the way for a more profound comprehension of their properties and possible uses.

Received 27th October 2023
Accepted 9th January 2024

DOI: 10.1039/d3ra07339d

rsc.li/rsc-advances

1. Introduction

Ferrite materials (MFe_2O_4) (M = Ni, Co, Mn, Mg or Zn) have gained prominence as multifaceted materials in recent years, offering a myriad of applications in cutting-edge technology. These spinel-structured oxide materials demonstrate exceptional physical, chemical, and magnetic properties, making them an essential component in diverse areas, such as electronics, communications, energy, and environmental sectors.[1–3] As a versatile material, Mg ferrite possesses unique magnetic and physical properties that render it useful across a wide array of applications.[4–7] Its high magnetic permeability, minimal magnetic losses, and remarkable magnetic stability make it ideal for magnetic cores,[8] while its high electrical resistivity and low thermal conductivity render it a promising material for energy conversion applications.[9]

Mg ferrite can adopt spinel structures in which divalent metal ions and trivalent metal distributed over the octahedral and tetrahedral sites.[10–12] Various techniques are in place to manipulate Mg ferrite's crystal structure and composition, which subsequently influences its magnetic and electrical properties. These include synthesis methods, doping, processing conditions, post-processing treatments, and ligand functionalization.[6,11,13–17] Adjusting the crystal structure and composition of Mg ferrite requires a deep understanding of its inherent properties and the invention of innovative synthesis and processing methods to customize its properties for specific utilities.[18,19] Numerous studies have highlighted the profound influence of thermal treatment on Mg ferrite's magnetic properties, attributing it to the distribution and magnetic ordering of cations over tetrahedral and octahedral sites.[20–22]

The captivating world of vibrational spectra of ferrites is a field that has seen considerable attention in scientific literature, thanks to the theoretical foundations laid by Waldron.[23,24] Waldron's model interprets the vibrations of this system using the point group T_d's irreducible representations. In principle, four IR active normal vibrations can be identified. The ν_1, the highest frequency, is associated with vibrations along the tetrahedral bonds. Meanwhile, the ν_2 frequency relates to vibrations along the octahedral bonds. The ν_3 and ν_4, on the other hand, represent the metal ion vibrations within their respective tetrahedral and octahedral environments. However, every model has its limitations. Waldron's model, as well as those proposed by White and De Angelis, have shown some challenges in interpreting certain characteristics observed in

Department of Chemistry, Section of Physical Chemistry, Taibah University, Madinah, 42353, Saudi Arabia. E-mail: talmutairi@taibahu.edu.sa

† Electronic supplementary information (ESI) available. See DOI: https://doi.org/10.1039/d3ra07339d

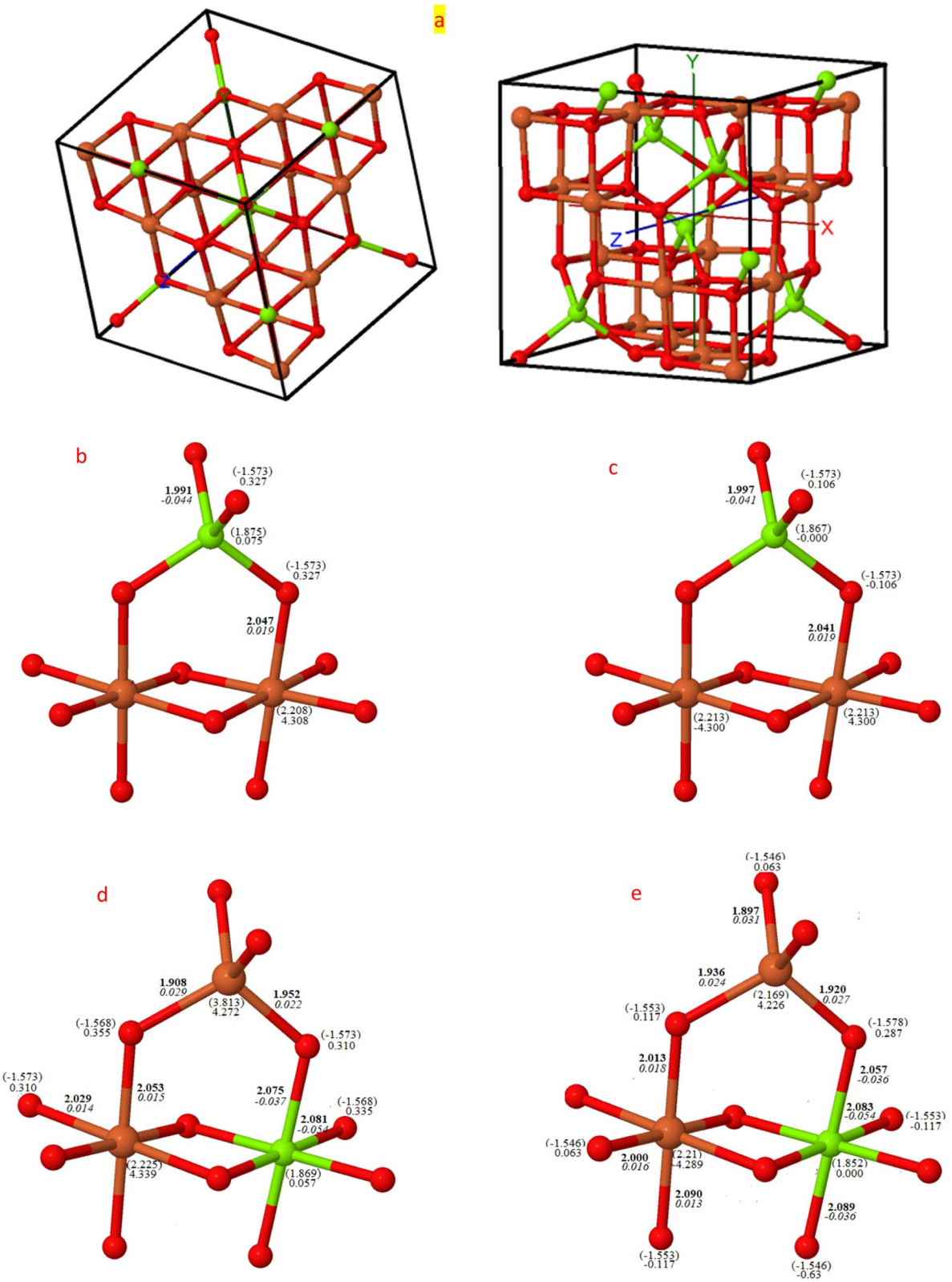

Fig. 1 Visual depiction of bond metrics for normal and inverse configurations: this figure provides (a) the conventional cubic cell (with 8 f.u. of $MgFe_2O_4$, delimited by solid black lines), and a schematic illustration of bond lengths (Å/bold), bond populations (|*e*|/*italic*), spin moment (|*e*|), and Mulliken charges (|*e*| in brackets) of non-equivalent atoms by symmetry for normal, (b) ferromagnetic (FM) and (c) antiferromagnetic (AFM), and inverse (d) FM and (e) AFM configurations. Atoms in red, orange, and green are for oxygen, iron and magnesium, respectively. Data is derived using B3LYP.

experimentally obtained spectra.[25] For instance, variations and splitting in the ν_1 and ν_2 bands reported by different researchers for distinct ferrites are perplexing phenomena yet to be fully explained. Moreover, inverse spinals add another layer of complexity. In these instances, each degenerate vibration may undergo splitting, leading to three separate frequency vibrations. This splitting primarily happens due to symmetry reduction. Numerous factors have been proposed to explain the splitting observed in the main bands, such as the Jahn–Teller distortions, the presence of a divalent metal in the octahedral complex, and the varying synthesis conditions.[25,26] The assignment of Raman modes further complicates the scenario as there are discrepancies between different studies.[10,27,28] Interestingly, the splitting of the five modes predicted by group theory for the cubic structure has also been observed.[16,29] A particularly elusive area is the phase transformation between various Mg ferrite configurations and their impact on frequencies, a topic rarely explored in literature using density functional theory (DFT).[7,30–33] This study aims to bridge this gap by examining the influence of cation distribution and magnetic ordering on the infrared (IR) and Raman spectra through DFT and using a hybrid functional. The ultimate goal is to provide theoretical insight into the phase change landscape of Mg ferrite, shedding light on the complexities of this fascinating field.

2. Computational methods

Theoretical investigations were performed within the framework of density functional theory (DFT) using the CRYSTAL17 software.[34] The functionals utilized in the calculations include the global hybrid functional B3LYP (20% of HF exchange),[35] PBE0 (25% of HF exchange),[36] and range-separated HSE06 (the fraction of HF exchange varies based on the distance between electrons),[37] which largely rectify the self-interaction error of pure DFT functionals. The choice of functionals is essential in DFT, as they significantly affect the predicted relative energies and thereby influence the interpretation of system stability and vibrational properties. B3LYP, in particular, has garnered widespread acceptance for its consistent performance in modeling a diverse array of chemical systems.[34,38,39] It merges the Becke three-parameter exchange with the Lee–Yang–Parr correlation functional, offering an extensively benchmarked and experimentally validated balance of accuracy and computational tractability. This has cemented its status as a preferred choice for computational studies, particularly when a reliable depiction of crystal behavior is paramount. Furthermore, B3LYP's ability to predict vibrational frequencies and other electronic properties is well-documented in comparative literature, underscoring its reliability and the rationale for its selection in this study. Gaussian-type functions were utilized for

Table 1 Comparative energy analysis of Mg ferrite spinel structure: this table details the total energy (in Hartree) E of Mg ferrite spinel structure ($Mg_{1-X}Fe_X$) [$Mg_XFe_{2-X}O_4$] for inversion factor $X = 0$ (normal), 0.5 (mixed), and 1 (inverse), calculated with different functionals. The bracketed E_R values signify the relative energy compared to the AFM inverse spinel structure

		$(X = 0)$		$(X = 0.5)$		$(X = 1)$	
Functionals		FM	AFM	FM	AFM	FM	AFM
B3LYP	E	−6057.0980	−6057.0950	−6057.0882	−6057.0988	−6057.0905	−6057.1059
	E_R	0.21	0.29	0.48	0.19	0.41	0.00
HSE06	E	−6055.9801	−6055.9767	−6055.9687	−6055.9784	−6055.9704	−6055.9845
	E_R	0.12	0.21	0.43	0.16	0.38	0.00
PBE0	E	−6055.9858	−6055.9823	−6055.9747	−6055.9841	−6055.9764	−6055.9901
	E_R	0.12	0.21	0.42	0.16	0.37	0.00

Table 2 Thermodynamic properties of Mg ferrite systems: Ttis table displays thermodynamic functions (eV per cell) at $T = 298.15$ K and $P = 0.10132500$ MPa for varied Mg ferrite systems. E_L signifies the energy per lattice cell (electronic energy), E_0 is the zero-point energy, E_T represents the thermal contribution to the vibrational energy, and S indicates entropy. All energies were computed at the B3LYP level. Bracketed values showcase relative energy compared to the ground state (AFM, $X = 1.0$)

	$X = 0$		$X = 0.5$		$X = 1$	
Energy	FM	AFM	FM	AFM	FM	AFM
E_L	−164822.0184	−164821.9344	−164821.7512	−164822.0390	−164821.8142	−164822.2312
E_0	0.9533	0.9406	0.9544	0.9510	0.9580	0.9602
E_T	0.3613	0.3668	0.3608	0.3624	0.3589	0.35819
S (meV per (cell K))	1.9515	1.9954	1.9414	1.9549	1.9208	1.9171
PV	0.0000975	0.0000974	0.0000968	0.0000961	0.0000958	0.0000957
TS	0.5818	0.5949	0.5788	0.5828	0.5727	0.5715
E_T + PV − TS	−0.2203	−0.2279	−0.2178	−0.2203	−0.2136	−0.2133
$E_L + E_0 + E_T$ + PV − TS	−164821.2855 (0.20)	−164821.2218 (0.26)	−164821.0147 (0.47)	−164821.3083 (0.18)	−164821.0698 (0.41)	−164821.4843 (0.00)

the all-electron basis set for all atoms involved.[40–42] The optimized structure enabled us to derive the IR and Raman active frequencies and intensities. We employed spin-polarized computations to investigate the effect of spin ordering on electronic and structural properties. In the ferromagnetic (FM) configuration, all magnetic moments were initially oriented in one direction. Conversely, in the antiferromagnetic (AFM) configuration, the magnetic moments between two Fe atoms in the unit cell were set to be antiparallel. The five thresholds, denoted as Ti, which govern the truncation criteria for the Coulomb and exchange infinite series, were set to 8 (T_1–T_4) and 16 (T_5). The self-consistent-field cycle used 10^{-8} and 10^{-10} Hartree energy convergence thresholds for optimization and vibration frequency calculations, respectively. The comprehensive optimization process, which involved lattice parameters and all atomic bases in the cell, used a root mean square (r.m.s.) displacement of 10^{-5} Å. The shrinking factors dictating the count of independent *k*-points employed in the sampling of the Monkhorst–Pack grid were configured to 88. The frequencies (wavenumber) ω_p were computed from second energy derivatives relative to atomic displacements u at the Γ point,[43,44] according to the following equations.

$$W_{ai,bj}{}^{\Gamma} = \frac{H^0_{ai,bj}}{\sqrt{M_a M_b}} \quad \text{where} \quad H^0_{ai,bj} = \frac{\partial^2 E}{\partial u^0_{ai}\, \partial u^0_{bi}} \tag{1}$$

In these equations, u denotes the atomic displacements of atom a, and b in the system, with the atomic mass, respectively. The i-th and j-th denote atomic coordinates. We were then able to determine the shift in frequencies due to isotopic substitutions at no additional computational cost by replacing the masses in eqn (1). The study used a coupled Perturbed–Hartree–Fock/Kohn–Sham method (CPHF/KS)[45,46] to calculate the integrated intensity for IR absorption and evaluated Raman intensities analytically.

3. Results and discussion

3.1 Bond lengths, charge and spin distribution, energy, and band structure

The consolidated visualizations of the converged structures of both normal and inverse magnesium ferrite in their two spin configurations, ferromagnetic (FM) and antiferromagnetic (AFM), are depicted in Fig. 1. Under both FM and AFM conditions, the cubic symmetry is preserved when $X = 0$, as demonstrated by the Mg–O and Fe–O bond lengths of approximately 4 × 1.99 Å and 6 × 2.04 Å. These measurements align closely with the recorded values of 1.99 Å and 2.02 Å, respectively.[19] The charge and spin distribution data highlight the ionic properties of the system, with the oxygen atom gaining a charge of −1.57|*e*|, while magnesium and iron atoms lose charges of 1.87|*e*| and 2.21|*e*| respectively. Bond populations are reported as −0.04 and 0.02 respectively. In the AFM configuration, there is a distinct alternating distribution of spin densities over the iron atoms in B-sites (4.3|*e*| α, −4.3|*e*| β), thereby maintaining a net zero spin per cell. However, in the FM configuration, all spins align parallel (4.3 α).

With the complete transformation to inverse structure, there is a clear distortion from the cubic form, resulting in two and three non-equivalent Fe–O and Mg–O bond lengths for FM ($X = 1$) and AFM ($X = 1$) respectively. This alters both the charge and spin distributions, as indicated in Fig. 1. The magnetic moment of iron in the A-site is smaller than in the B-site by approximately 0.06|*e*|, and inversely, the magnetic moment of Mg in the B-site is lower than in the A-site by 0.02|*e*| in the FM configuration, but this becomes zero in both AFM structures. The FM

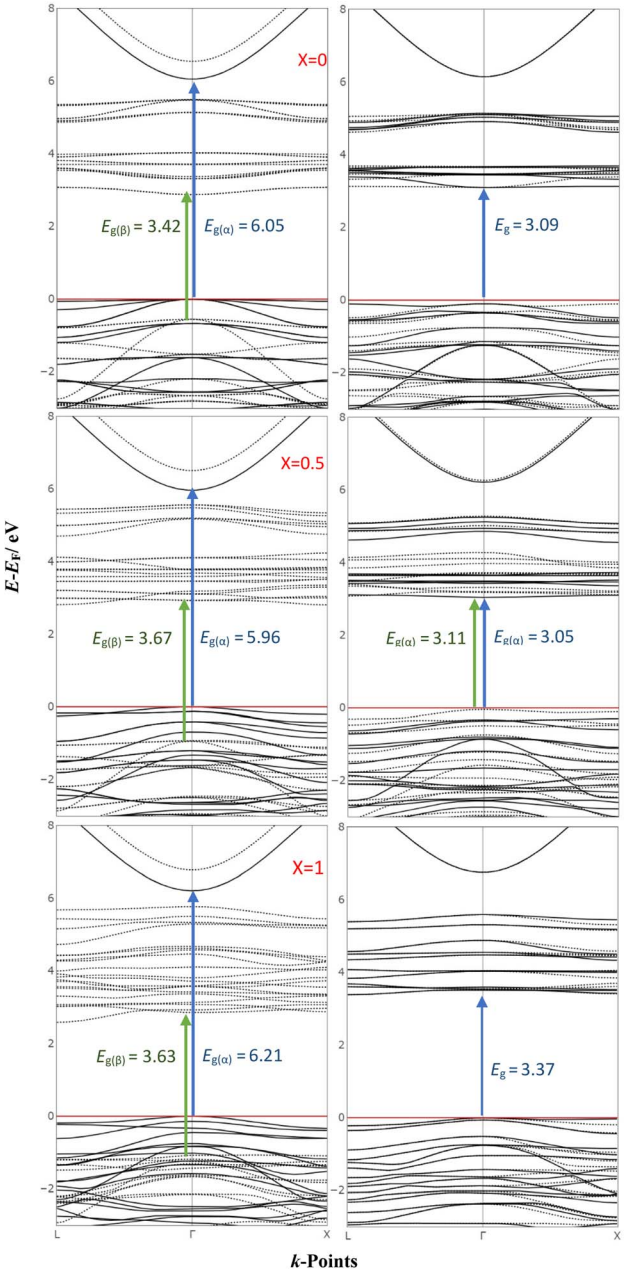

Fig. 2 Band structures of Mg ferrite in FM and AFM configurations: this figure shows the band structures of Mg ferrite in FM (left panel) and AFM (right panel) configurations as calculated with B3LYP for varying degrees of inversion. The red horizontal line denotes the Fermi level set to zero, while continuous and dotted black lines represent the α and β energy bands, respectively.

lattice parameter when $X = 0$ is 8.51 Å, which decreases to 8.46 Å when inverted to FM ($X = 1$), closely matching the measured value of 8.44 Å.[47]

The relative energy difference among the six optimized structures was analyzed using three functionals and is presented in Table 1. The most stable configuration was determined to be the inverse structure with AFM arrangements.[27,48] MFO is an antiferromagnetic material, with magnetic moments aligned in an antiparallel orientation, resulting in a net magnetic moment of zero. This is consistent with experimental observations of zero magnetization at a Curie temperature of 738 K.[49] This antiferromagnetic behavior is attributed to its inverse spinel structure, where the magnetic moments of iron ions on tetrahedral sites are compensated by the magnetic moments of iron ions on octahedral sites due to the nonmagnetic nature of magnesium atoms. The energy difference between FM and AFM in the ($X = 1$) arrangement was found to be notably high at 0.41 eV (B3LYP), even considering the free energy inclusive of zero-point energy (Table 2).

The band structures of MFO in their FM configurations were compared to their corresponding AFM configurations, as illustrated in Fig. 2. The influence of inversion on the electronic structure was minimal, with the band gap increasing by 0.16 eV for α bands and 0.21 eV for β bands in FM and by 0.28 eV in AFM upon transitioning from the normal to inverse structure. The band gaps of the AFM structures in this study closely match the measured value of 2.48 eV for samples calcinated at 700 °C,[50] and 2.38 eV (ref. 51) for those calcinated at 550 °C. The variations in band gaps with changing temperatures may be related to cation disorder within the crystal or existing defects such as oxygen vacancies.[30,52] In the FM configuration ($X = 0$ and 1), the band gaps along the α and β spins are open at the gamma point (direct band gap), while only the α gap is direct for $X = 0.5$. In the AFM configuration, the shift between the α and β bands is minor, resulting in virtually identical band gaps.

3.2 Spectroscopic characterization: investigating crystal structures *via* Raman and infrared spectroscopy

Raman and Infrared spectroscopy serve as robust methodologies for comprehensively probing vibrational properties in various materials. These techniques provide invaluable

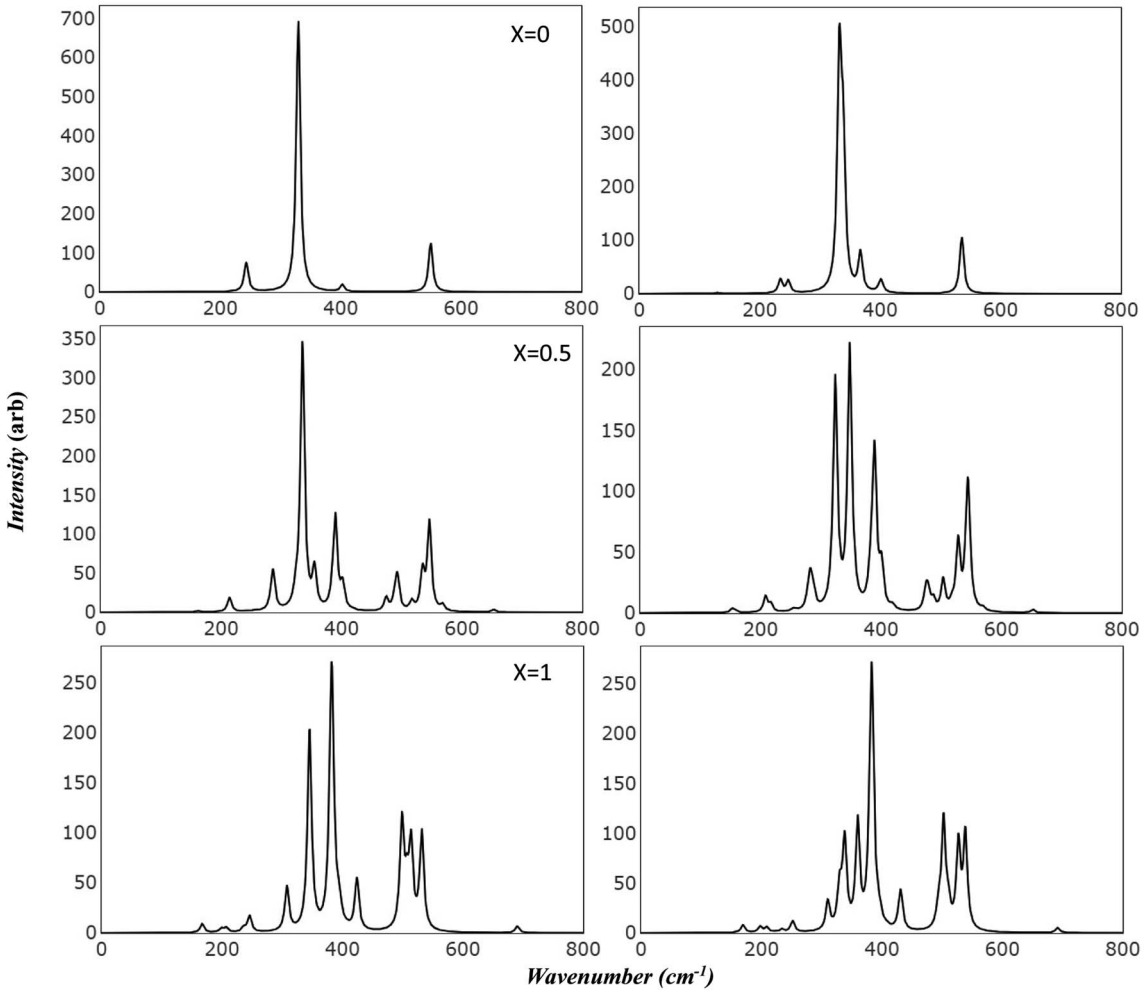

Fig. 3 Simulated infrared spectra of Mg ferrite by B3LYP: this figure displays B3LYP simulated infrared spectra of Mg ferrite ($X = 0.0, 0.5, 1.0$) with its two-order magnetic configuration, where left panels refer to FM and right panels refer to AFM.

perspectives on the crystal structure, chemical composition, and defective characteristics by scrutinizing the frequency and intensity of the scattered light. Additionally, they can be employed to investigate the impact of extrinsic factors, such as temperature and pressure, on the vibrational characteristics of the material under study. Through meticulous observation of spectral changes under diverse conditions, researchers can achieve a more profound comprehension of the physical principles that govern the magnetic and electrical attributes of Mg ferrite. Importantly, the simulated spectra has introduced a powerful tool in scientific resources. This facilitates precise characterization of spectral features, effectively avoiding numerous confounding factors such as preparation methods, temperature variations, defects, and intrinsic structural disorder, which may otherwise make the analysis unclear.

Fig. 3 presents the simulated vibrational frequencies and intensities of Mg ferrite geometries ($X = 0.0, 0.5, 1.0$) within two spin configurations: ferromagnetic (FM) and antiferromagnetic (AFM). All spectra are computed at the B3LYP level and visualized using a pseudo-Voigt function, a linear combination of Lorentzian and Gaussian functions, with a full width at half maximum of 8 cm^{-1}. For the FM configuration ($X = 0.0$), four triply degenerate T_{1u} modes, predicted by group theory analysis for the *Fd*3*m* space group structure, are discerned. These four peaks are observed at 243, 330, 403, and 550 cm^{-1}, with the peak at 330 cm^{-1} showcasing an exceptionally high intensity compared with the others. The two lowest frequency peaks are subject to disagreement across different papers regarding their detection and precise location.[10] In its AFM counterpart, the intense peak is slightly affected by the new configuration (332 cm^{-1}), with a small peak appearing at 338 cm^{-1}. Additional minor peaks emerge at 129 and 367 cm^{-1}, and the low-frequency peak (243) splits into two peaks at 234 and 247 cm^{-1}. At higher frequencies, peaks are observed at 400 and 403 cm^{-1}, and one at 536 cm^{-1}, marking a shift of 14 cm^{-1} compared to 550 cm^{-1} in FM. The FM spectra analysis reveals that the peak at 243 cm^{-1} is associated with the bending mode of the Fe–O–Mg bond, and the subsequent two peaks at 330 and 403 cm^{-1} are connected to the bending bond of O–Mg–O and Fe–O–Mg. The highest frequency band at 550 cm^{-1} signifies a combination of the stretching mode of the Mg–O bond and the bending mode of the Fe–O–Mg bond.

In the AFM configuration, the peak at 129 cm^{-1} involves the bending modes of Fe–O–Mg and Fe–O–Fe, and the subsequent two peaks at 234 and 247 cm^{-1} entail the bending mode of Fe–O–Mg, sustaining the same modes as the 243 cm^{-1} in FM. The peak at 332 cm^{-1} and its shoulder at 338 cm^{-1} are more correlated than other modes, as they comprise the stretching mode of Fe–O–Fe and bending modes of O–Mg–O, Fe–O–Fe, and Fe–O–Mg. The final modes (400, 403, 536 cm^{-1}) involve the bending and stretching of O–Mg–O and Fe–O–Mg bonds.

The IR spectra reflect splitting upon transitioning from normal to complete inverse structure. For FM ($X = 1.0$), low frequency region reveals a small peak at 167 cm^{-1}, followed by peaks at 199, 207, and 246 cm^{-1}, which correspond to the 243 cm^{-1} peak in FM ($X = 0$). These peaks are associated with the bending mode of both cations, except for the modes at 207 and 246 cm^{-1}, which relate to the iron cation, O–Fe–O. The peak at 246 cm^{-1} appears with small shoulders at 236 cm^{-1}, signifying a combination of bending modes of O–Fe–O, FeO–Mg– and Fe–O–Fe. At moderate frequencies, high-intensity peaks appear at 308 cm^{-1}, encompassing the bending of all cations, and 346 cm^{-1}, marking the stretching mode of O–Fe–O. A peak at 383 cm^{-1} has the highest intensity and involves a complex mode of Mg–O stretching and Fe–O–Mg bending. The peak at 424 cm^{-1} exhibits stretching modes for Fe–O and Fe–O–Mg. In the high-frequency region, a group of split peaks are observed (499, 507, 514, and 532 cm^{-1}), corresponding to the unsplit peak at 550 cm^{-1} in FM ($X = 0$). The mode at 499 cm^{-1} is linked to the stretching of Fe–O and Mg–O bonds and the bending of Fe–O–Fe. The peaks at 507 and 514 cm^{-1} relate to the stretching of Mg–O and the bending of O–Mg–O, respectively, and the one at 532 cm^{-1} involves the stretching of Fe–O bonds.

The highest frequency peak at 690 cm^{-1} appears in an otherwise flat area in the normal spectra, making it a potential marker for identifying the inverted structure. This mode involves the stretching of Fe–O and the bending of Fe–O–Mg and Fe–O–Fe. Baraton *et al.* detected this high frequency peak for Mg ferrite at 700 cm^{-1}, alongside the two main peaks (ν_1, ν_2) at 581 and 424 cm^{-1}, and found that it becomes more pronounced as the Mg content increases.[10]

Table 3 presents a comparison of the frequencies observed in FM and AFM orderings within an inverted structure. A marked shift is observed for AFM (where $X = 1$) when compared to its FM counterpart. Specifically, the peaks observed at 252, 431, 527, and 539 cm^{-1} in AFM display an upward shift by 6, 7, 13, and 7 cm^{-1}, respectively, when compared to the corresponding FM frequencies (246, 424, 514 and 532 cm^{-1}). In the FM

Table 3 Frequency comparison of inverse structure with two-spin ordering: this table contrasts the simulated frequencies of an inverse structure with its two-spin ordering (FM and AFM)

Sy	Frequencies (cm^{-1}) FM ($X = 1$)	Frequencies (cm^{-1}) AFM ($X = 1$)	Shifts (cm^{-1})
B_{2u}	167	169	+2
B_{3u}	199	198	−1
B_{2u}	207	209	+2
B_{1u}	236	234	−2
B_{3u}	246	252	+6
B_{1u}	308	310	+2
B_{2u}	346	338	−8
		360	
B_{3u}	381	382	−1
B_{1u}	383	384	−1
B_{3u}	394	394	0
B_{2u}	395	397	+2
B_{1u}	408	408	0
B_{3u}	424	431	+7
B_{3u}	499	494	−5
B_{1u}	507	503	+4
		511	
B_{1u}	514	527	+13
B_{1u}	529	529	0
B_{2u}	532	539	+7
B_{1u}	690	692	+2

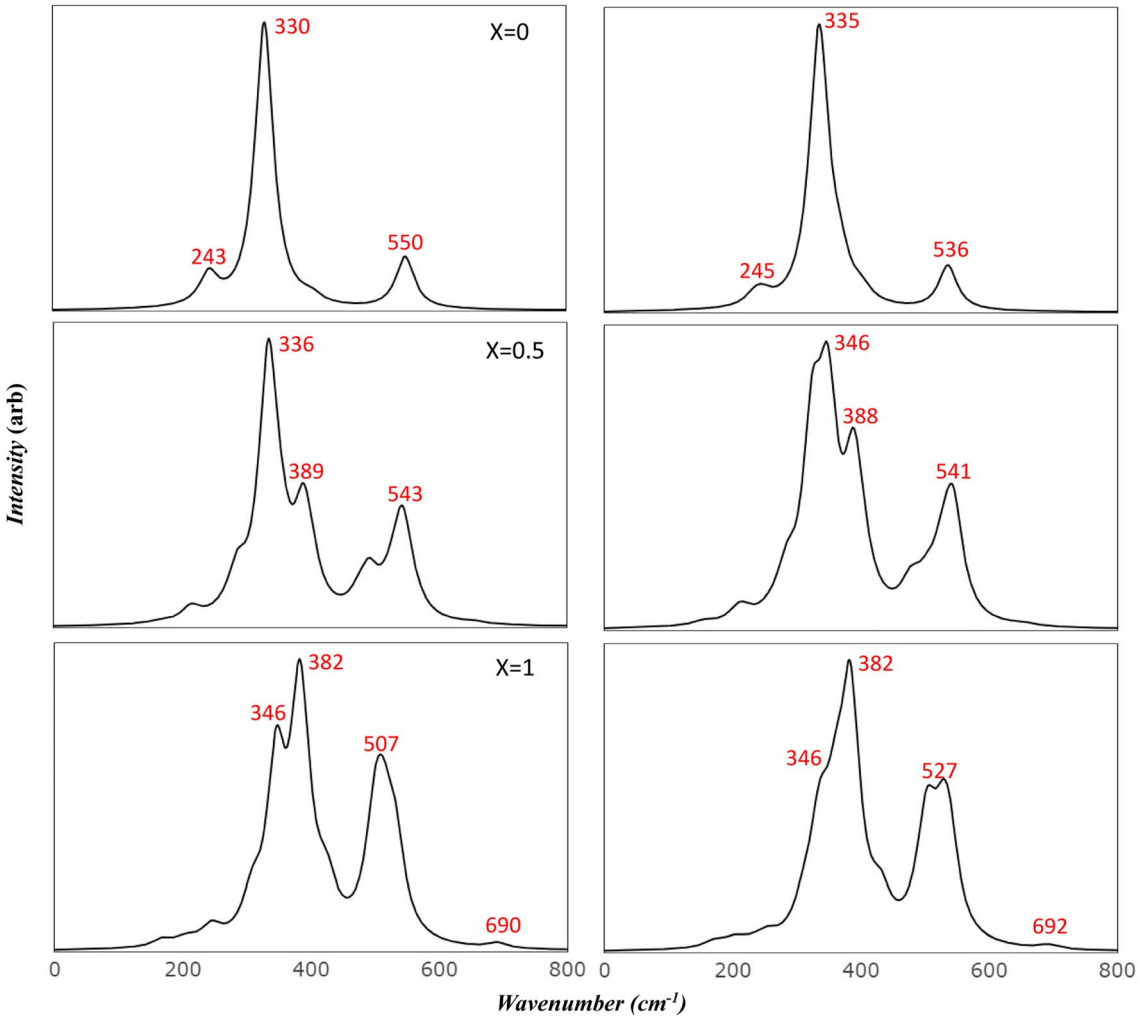

Fig. 4 Comparison of simulated IR spectra of Mg ferrite: this figure compares the simulated IR spectra of Mg ferrite ($X = 0.0, 0.5, 1.0$) in its two-spin order using a Full Width at Half Maximum (FWHM) of 35 cm^{-1}.

Table 4 Analysis of normal Mg ferrite IR modes frequencies: this table compares the frequencies of the IR modes of normal Mg ferrite as previously documented in literature

Vibrational modes (cm^{-1})	Ref. 23	Ref. 14	Ref. 47	Ref. 21	Ref. 54	Ref. 10	Ref. 28		Ref. 51	
							200 °C	1000 °C	550 °C	1000 °C
ν_1	565	561	566	606	574	581	552	542	539	536
ν_2	406	437	409	458	409	424	424	418	395	402
ν_3									350	360
ν_4										

spectrum, the peak at 346 cm^{-1} diminishes to half its original intensity when it shifts to 338 cm^{-1} in the AFM spectrum. This shift is accompanied by the emergence of a new peak at 360 cm^{-1}. The group of FM peaks at 499, 507, 514, 532 cm^{-1} exhibit a significant shift in the AFM spectrum, appearing at 494, 511, 527 and 539 cm^{-1}, respectively. Their intensities also decrease by half. A dominant peak emerges at 503 cm^{-1} in the AFM spectrum, displaying a high intensity. This peak is associated with the stretching mode of both Fe–O and Mg–O bonds. The two modes at 494 and 511 cm^{-1} blend with the 503 cm^{-1} peak, resulting in a broad, dominant peak.

To more accurately mimic the experimental broadening of peaks and create a more representative image, we adjusted the full width half maximum value from 8 to 35 cm^{-1}. This was done using a linear combination of Lorentzian curves to derive the pseudo-Voigt functional form, as depicted in Fig. 4. The

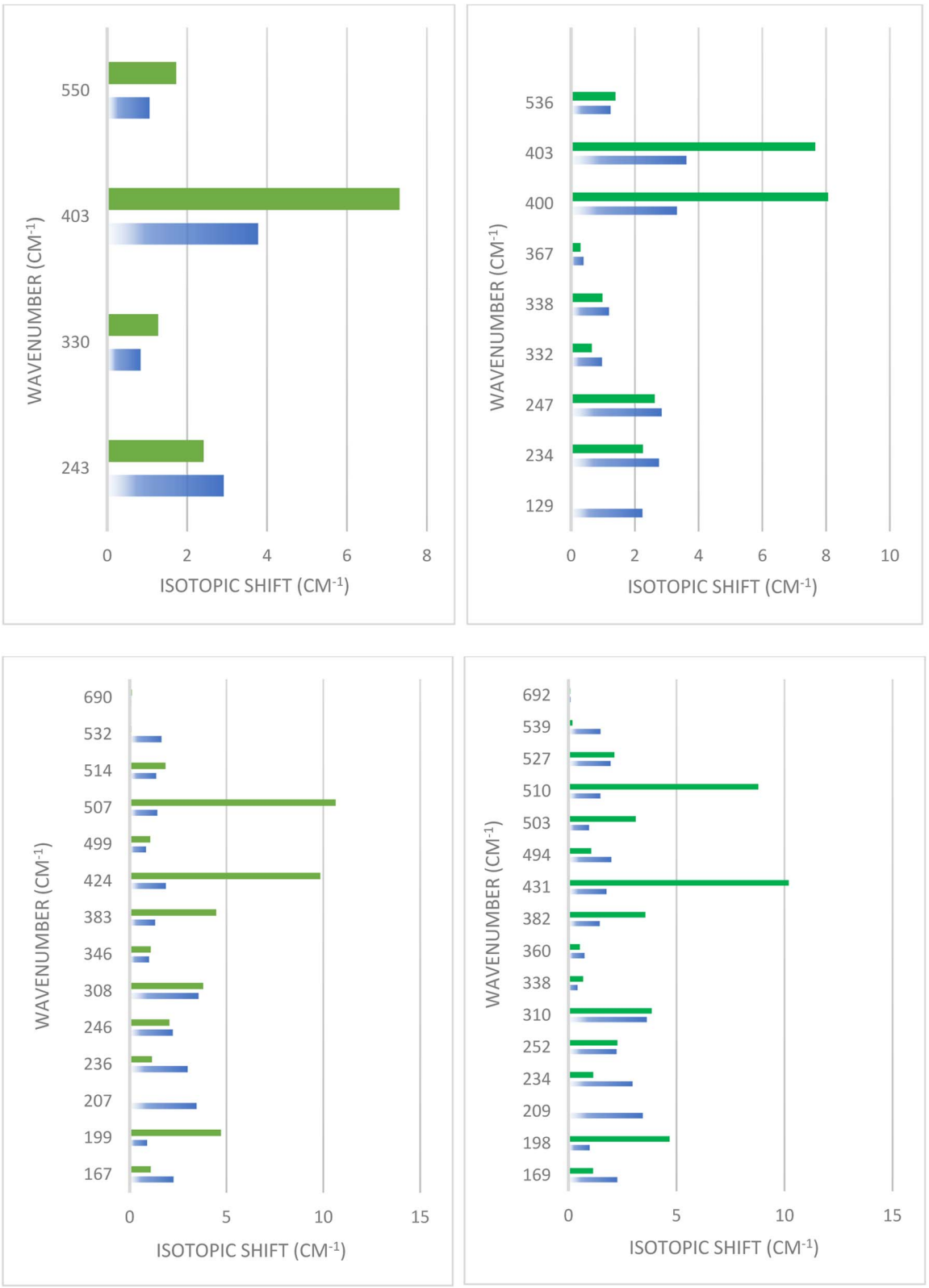

Fig. 5 Simulated isotopic shifts in Mg ferrite: this figure shows the simulated isotopic shifts resulting from $^{56}Fe \rightarrow {}^{58}Fe$ and $^{24}Mg \rightarrow {}^{26}Mg$ substitution for Mg ferrite ($X = 0.0$ (top panel), 1.0 (below panel)) in its two-spin configuration. Blue bars represent Fe atom and green bars represent the Mg atom.

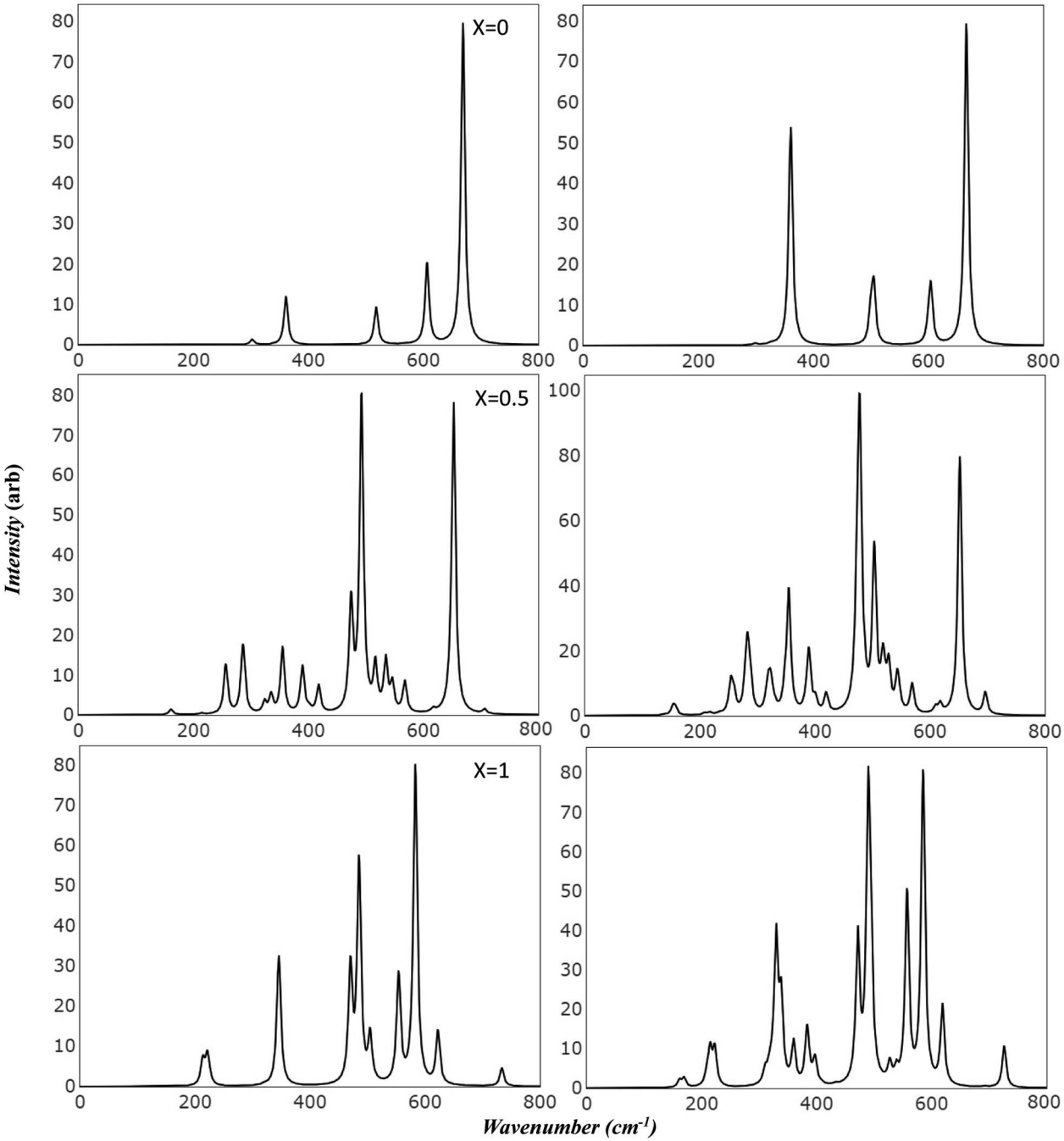

Fig. 6 Simulated Raman spectra of Mg ferrite by B3LYP: this figure presents B3LYP simulated Raman spectra of Mg ferrite ($X = 0.0, 0.5, 1.0$) with its two-order magnetic configuration, where left panels refer to FM and right panels refer to AFM.

results we obtained showed a satisfactory agreement with the most commonly reported values for ν_1 and ν_2, as listed in Table 4. These results also provided an explanation for the fewer features observed in the experimental data.

Previous studies have reported the splitting of IR peaks in MFO due to deformation from a cubic to a non-cubic structure. For instance, Waldron reported ν_1 and ν_2 at 565 and 406 cm^{-1}, respectively, along with additional peaks at 380, 430, and 735 cm^{-1}.[23] Heiba *et al.* also reported a split in the main ν_1 and ν_2 modes, with the seven frequencies in their study recorded at 406, 419, 436, 481, 493, 582, and 667 cm^{-1}.[53] Their findings indicated that these frequencies were influenced by the ratio of cations. The frequency at 667 cm^{-1}, which had a very low intensity, was not identified in some of their samples, aligning with our findings. Frequencies lower than 400 cm^{-1} were not reported in their study due to the limitations of their instrument.

In order to delve deeper into the contribution of cations in the observed modes, we computed the spectra of isotopic substitutions ($^{56}Fe \rightarrow {}^{58}Fe$ and $^{24}Mg \rightarrow {}^{26}Mg$). As seen in Fig. 5,

Table 5 Assignment of Raman modes in Mg ferrite: this table compares the Raman modes assignments for Mg ferrite as calculated in the current study and as previously reported

								Current study					
				Ref. 28		Ref. 16		($X = 0$)			($X = 1$)		
Sy	Ref. 55	Ref. 27	Ref. 10	200 °C	1000 °C	500 °C	Ref. 29	Sy	FM	AFM	Sy	FM	AFM
T_{2g} (1)	217	217	209	202	216	217	215	T_{2g} (1)	302	298	B_{3g}	213	215
											A_g	221	222
											B_{2g}	*224*	*224*
E_g	333	329	326	307	331	326	335	E_g	361	361	B_{1g}	*316*	329
											B_{2g}	*320*	338
											B_{3g}	*332*	360
						367					B_{1g}	*345*	384
											A_g	346	397
T_{2g} (2)	486	480	475	462	483	487	400	T_{2g} (2)	518	505	B_{2g}	470	472
											A_g	485	490
							480			500	B_{3g}	505	503
T_{2g} (3)	554	548	535	499	546	550	560	T_{2g} (3)	607	605	B_{2g}	554	557
											A_g	583	585
	646					590					B_{3g}	622	619
A_{1g}	715	704	700	693	707	630	670	A_{1g}	669	667	A_g	734	726
						703	715						

the vibrations of cations in their sites are highly correlated, making it challenging to interpret the spectra by categorizing the observed modes into A-site and B-site. In both FM and AFM ($X = 0$), the most noticeable shift was observed for the normal mode at approximately 400 cm^{-1}. The largest shift occurred with the ^{26}Mg substitution, which was 7–8 cm^{-1}, while the ^{58}Fe substitution resulted in a shift of approximately 3.5 cm^{-1}. In FM and AFM of ($X = 1$), where all the Mg atoms transition to the octahedral site, a significant shift was also observed with the ^{26}Mg substitution at 424 and 507 cm^{-1} mode in FM and 431 and 510 cm^{-1} modes in AFM. This shift was considerable, at about 10 cm^{-1}. The modes at (199, 308, and 383 cm^{-1}) in FM and their corresponding modes at (198, 310, and 382 cm^{-1}) in AFM, shifted with ^{26}Mg by 3.6–4.7 cm^{-1}, indicating the influence of these modes by the lighter atom (Mg). Moreover, the ^{58}Fe substitution also shifted the two modes at 308 and 207 cm^{-1} in FM, and the modes at 310 and 209 cm^{-1} in AFM by 3.5 cm^{-1}.

In the examination of scattered Raman (Fig. 6), the five modes predicted by group theory are discerned in FM ($X = 0.0$) at the following frequencies: 669 cm^{-1} for A_{1g}; 607, 518, and 302 cm^{-1} for triply degenerate T_{2g} symmetry; and 361 cm^{-1} for doubly degenerate E_g symmetry. Analysis of these modes reveals that the peaks at 302 cm^{-1} and 607 cm^{-1} encompass all the cations, specifically including the bending mode of O–Mg–O and Fe–O–Mg, in addition to the Fe–O–Fe bending detected at 606.6 cm^{-1}.

The peak at 361 cm^{-1} implicates the stretching mode of Fe–O–Fe, O–Fe–O, and Fe–O–Mg, along with the bending mode of O–Mg–O and Fe–O–Mg. The peak at 518 cm^{-1} solely corresponds to the stretching mode of O–Mg–O and Fe–O–Mg bonds. The peak with the highest intensity and frequency, at 667 cm^{-1}, is associated with the stretching mode of Mg–O and the bending mode of Fe–O–Mg. The impact of AFM spin ordering on Raman spectra is evident in both frequencies and intensities. For example, the peak at 302 cm^{-1} is shifted by 4 cm^{-1} (to 298 cm^{-1}) and its intensity is halved, while the second peak at 361 cm^{-1} remains stationary but its intensity increases fivefold. The most significant shift is observed with the 518 cm^{-1} peak, which shifts to a lower frequency by 13 cm^{-1} (to 505 cm^{-1}) with a doubling in intensity. This peak combines with a shoulder at 500 cm^{-1}, leading to peak broadening. Minor shifts to lower frequencies are seen with 607 and 669 cm^{-1}, by about 2 cm^{-1}, accompanied by a minor decrease in their intensities.

Upon conversion to an inverse structure, the spectra undergo splitting over a broad region and show emerging new peaks, indicative of the deformation of the cubic structure. Starting with FM ($X = 1$), the spectra display ten peaks appearing in the entire calculated region. New twin peaks emerge at 213 and 221 cm^{-1}, with small intensities related to the bending mode of O–Mg–O, Fe–O–Fe, and O–Fe–O. The peak at 346 cm^{-1}, shifted from the corresponding doubly degenerate peak in FM ($X = 0$) at 361 cm^{-1} by 15 cm^{-1}, displays a high correlation between cations, involving similar modes to those found at 361 cm^{-1}.

The mid-range features three split peaks at 470, 485, and 505 cm^{-1}. The peaks at 470 and 485 cm^{-1} are related to the stretching mode of Fe–O–Mg and O–Fe–O, and the second peak at 485 cm^{-1} additionally involves the bending mode of O–Fe–O and Fe–O–Fe. The third peak at 505 cm^{-1} is correlated to iron only, involving the stretching mode of both Fe–O–Fe and O–Fe–O. Another group of three peaks at 554, 583, and 622 cm^{-1} appear in the high-frequency region, along with a small peak at the edge of the spectra at 734 cm^{-1}. The peak at 554 cm^{-1} resonates with the same stretching modes as the 470 cm^{-1} peak, but also includes the bending of O–Fe–O. Meanwhile, the 583 and 622 cm^{-1} peaks incorporate the same stretching modes as the 505 cm^{-1} peak, but with the additional bending of Fe–O–

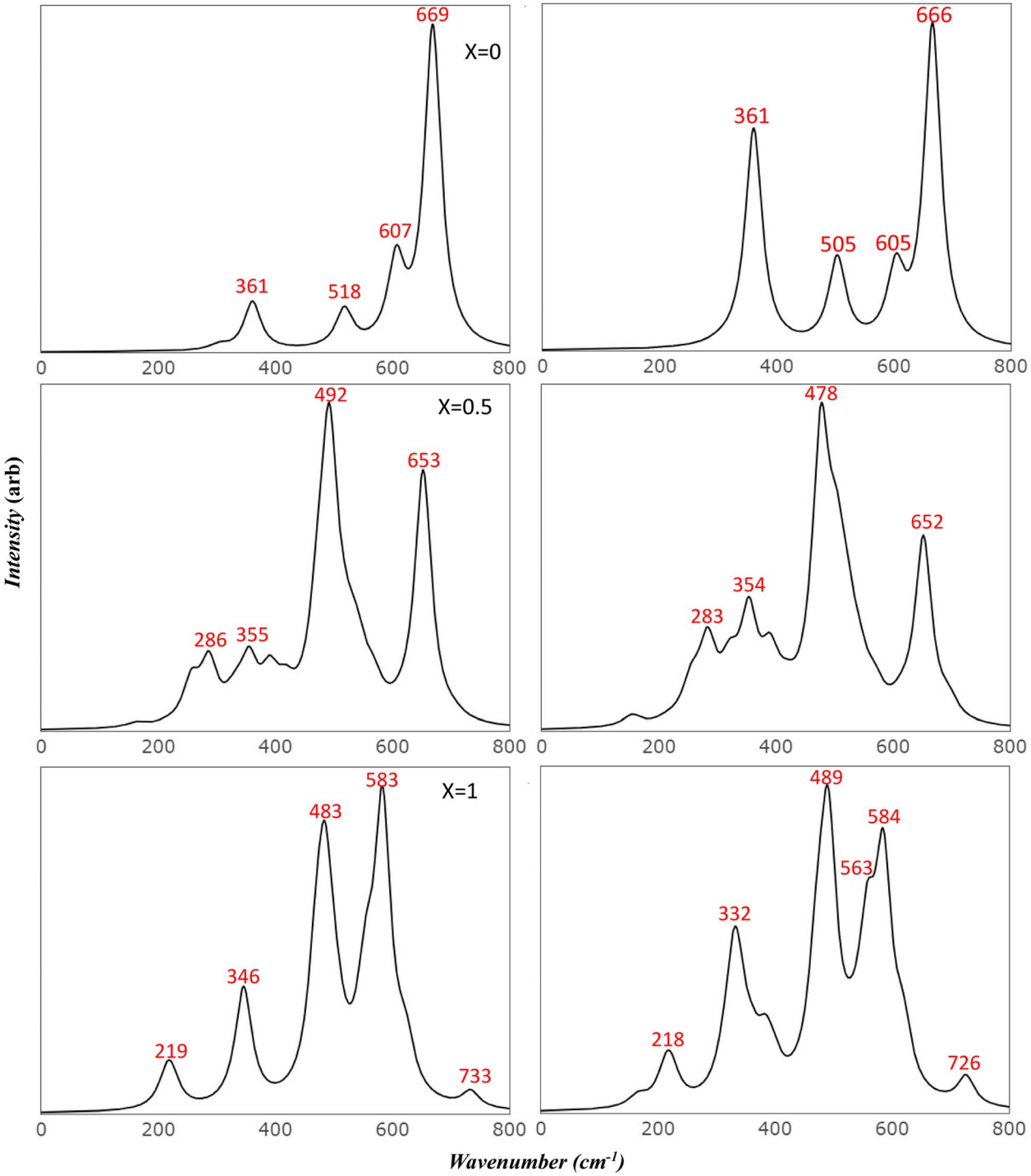

Fig. 7 Comparison of simulated Raman spectra of Mg ferrite: this figure contrasts the simulated Raman spectra of Mg ferrite ($X = 0.0, 0.5, 1.0$) in its two-spin order using a Full Width at Half Maximum (FWHM) of 35 cm^{-1}.

Fe and O–Mg–O, respectively. The peak at 734 cm^{-1} is related to the bending of Fe–O–Mg and Fe–O–Fe and the stretching of the Fe–O bond.

Alterations in spin arrangement in AFM ($X = 1$) also affect the Raman spectra, prompting shifts for most peaks and activating only three peaks due to slight deformation. Small new twin peaks appear at 162 and 169 cm^{-1}, and another at 527 cm^{-1}. No further splitting occurs for other peaks; instead, they undergo shifts as listed in Table 5. One of the most notable features in AFM spectra is the significant intensity increase of a group of peaks in the region of 300 cm^{-1} (329, 338, 360, 384, and 397 cm^{-1}), four of which had almost zero intensity in FM. The small peak at 503 cm^{-1} merges with the 490 cm^{-1} peak to form one broad peak. The peak at 734 cm^{-1} in FM can be seen

as an indication of the present inverse structure as it stands in a flat region in the normal spectra. Its large shift (8 cm^{-1}) with the change in spin order can be useful for tracking phase changes under experimental conditions. Most of the studies reported in Table 5 detected this peak.

The comparison of the obtained frequencies for both normal and inverted structures with available experimental data reveals a better alignment with the inverted structure. The breadth of the experimental peaks can be represented by resetting the full width half maximum value from 8 to 35 cm^{-1}, as executed in the IR section (Fig. 7). Wang *et al.*[55] predicted seven modes at frequencies of 217, 333, 390, 486, 554, 646, and 715 cm^{-1}. These predictions are detailed in Table 5. The researchers attributed the additional peak at 646 cm^{-1} to the order–disorder effect within the structure. However, they provided no further explanation for the presence of the peak at 390 cm^{-1}, which is also found in the simulated AFM Mg ferrite spectra (refer to Table 5). Our simulated spectra, with a FWHM of 35 cm^{-1}, bear a significant resemblance to those of Wang *et al.* Frequencies of the modes are found at 218, 332, 489, 563, 584, 619, and 727 cm^{-1}. The minor peak at 618 cm^{-1} merges with the 583 cm^{-1} peak in our study. The low intensity of these peaks could account for their absence in most of the studies listed in Table 5.[10,27,28] Nakagomi *et al.* predicted seven modes similar to those identified by Wang *et al.* Yet, they attributed the peak at 670 cm^{-1} to the substitution of iron (Fe) atoms at tetrahedral sites with magnesium (Mg) atoms.[29] They proposed that the substantial mass difference between Fe^{3+} and Mg^{2+} ions cause the A_{1g} mode to split into two: one being attributable to Mg^{2+} (715 cm^{-1}) and the other to Fe^{3+} ions (670 cm^{-1}). They quantified the ion distribution at the tetrahedral sites based on the fluctuation in the integrated intensity of both modes relative to the total spectrum. Feng *et al.* identified a clear splitting into eight modes, including E_g and T_{2g} (3), which further split into four peaks. They attributed the two highest peaks to A_{1g}.[16] Their frequency values align with our findings, but the assignments they reported do not. The peak at 619 cm^{-1}, which resulted from the T_{2g} (3) split in our study, closely matches their value at 630 cm^{-1}. It's evident that the deformation from the cubic structure in inverse spinel leads to the degeneration of most modes and activates new modes in the Mg ferrite spectra. This finding aligns with experimental results[10] and suggests that the assignments provided in existing literature need to be reassessed considering our simulated data.

4. Conclusion

This study delves into a comprehensive theoretical analysis based on density functional theory, examining the influence of inversion degree and spin arrangement of magnesium ferrite on multiple attributes including geometry, energy, electronic structure, and the frequencies and intensities of both IR and Raman spectra. We found that the inverse structure with antiferromagnetic order emerges as the ground structure, with relative energy being 0.21 and 0.41 eV (B3LYP) compared to the ferromagnetic order of ($X = 0$) and ($X = 1$), respectively. Our findings uncover the profound effect of inversion on the lattice structure, leading to deformation that significantly impacts the calculated IR and Raman spectra, inducing noteworthy shifting and splitting. The four IR frequencies with T_{1u} symmetry calculated for the typical cubic structure of ($X = 0$) (243, 330, 403, and 550 cm^{-1}) split over a wide spectral region upon inversion ($X = 1$). These frequencies are further influenced by the spin order, leading to a significant shift that provides valuable insights into phase transition under varying experimental conditions. Our isotopic calculations reveal an intricate relationship between the Mg and Fe vibrational modes. Despite the large correlation detected, some specific modes are predominantly influenced by the lighter Mg atom rather than the Fe atom, attributable to the substantial mass discrepancy, irrespective of the degree of inversion. This results in a significant shift (7–10 cm^{-1}) obtained by Mg^{26} substitution with (403 cm^{-1}) in the normal structure and (424, 507 cm^{-1}) alongside corresponding modes (431, 510 cm^{-1}) in FM and AFM, respectively, in the inverse structure. This can be construed as evidence of this mode's correlation to the Mg cation. Even though the IR peak at 690 cm^{-1} is of low intensity, its detection can be attributed to the inverse structure since no corresponding peak exists in this region in the normal phase. The simulated Raman spectra, which demonstrate splitting, elucidate a substantial amount of experimental data that detected more than five modes for Mg ferrite. Consequently, the provided assignments were reevaluated, taking into account the reduction in symmetry caused by lattice deformation. Similar to IR, the unique peak detected at the highest frequency region (727 cm^{-1}) in Raman spectra can be considered as evidence for inverting the spinel structure. Unlike the 690 cm^{-1} peak in IR, this peak has a detectable intensity and is observed in most of the experimental data. In summary, this study invites us into a world where the inversion degree and spin arrangement of magnesium ferrite display substantial impacts on the material's properties. The findings not only contribute to the scientific understanding of these materials but also open up new alleys for exploration, fostering future developments in material science.

Author contributions

Dr Tahani Saad Almutairi contributed in conceptualizing and designing the study, curating data, performing the formal analysis, leading the investigation, drafting the manuscript, and revising it critically for important intellectual content.

Conflicts of interest

There are no conflicts to declare.

Acknowledgements

The author extends his thanks to Taibah University and the Deanship of Scientific Research for their generous support, offering both essential facilities and an encouraging research atmosphere that contributed to conducting this study within the Department of Chemistry.

References

1 A. Goldman, *Modern Ferrite Technology*, Springer Science & Business Media, 2006.
2 R. Ranga, A. Kumar, P. Kumari, P. Singh, V. Madaan and K. Kumar, *Mater. Charact.*, 2021, **178**, 111269.
3 K. K. Kefeni, T. A. Msagati and B. B. Mamba, *Mater. Sci. Eng., B*, 2017, **215**, 37–55.
4 N. R. Su, P. Lv, M. Li, X. Zhang, M. Li and J. Niu, *Mater. Lett.*, 2014, **122**, 201–204.
5 W. Tang, Y. Su, Q. Li, S. Gao and J. K. Shang, *Water Res.*, 2013, **47**, 3624–3634.
6 P. Hankare, S. Jadhav, U. Sankpal, R. Patil, R. Sasikala and I. Mulla, *J. Alloys Compd.*, 2009, **488**, 270–272.
7 J. Zhang, M. Yan, G. Sun, X. Li and K. Liu, *J. Alloys Compd.*, 2021, **889**, 161673.
8 S. Verma, P. A. Joy, Y. B. Khollam, H. S. Potdar and S. B. Deshpande, *Mater. Lett.*, 2004, **58**, 1092–1095.
9 Y. Hou, F. Zuo, A. Dagg and P. Feng, *Angew. Chem., Int. Ed.*, 2013, **52**, 1248–1252.
10 M. I. Baraton, G. Busca, V. Lorenzelli and R. J. Wllley, *J. Mater. Sci. Lett.*, 1994, **13**, 275–279.
11 N. Sivakumar, A. Narayanasamy, J. M. Greneche, R. Murugaraj and Y. S. Lee, *J. Alloys Compd.*, 2010, **504**, 395–402.
12 M. Gateshki, V. Petkov, S. K. Pradhan and T. Vogt, *J. Appl. Crystallogr.*, 2005, **38**, 772–779.
13 Y.-L. Liu, Z.-M. Liu, Y. Yang, H.-F. Yang, G.-L. Shen and R.-Q. Yu, *Sens. Actuators, B*, 2005, **107**, 600–604.
14 A. Pradeep, P. Priyadharsini and G. Chandrasekaran, *J. Magn. Magn. Mater.*, 2008, **320**, 2774–2779.
15 S. Jesus Mercy, D. Parajuli, N. Murali, A. Ramakrishna, Y. Ramakrishna, V. Veeraiah and K. Samatha, *Appl. Phys. A: Mater. Sci. Process.*, 2020, **126**, 1–13.
16 Y. Feng, S. Li, Y. Zheng, Z. Yi, Y. He and Y. Xu, *J. Alloys Compd.*, 2017, **699**, 521–525.
17 V. Šepelák, D. Baabe, F. J. Litterst and K. D. Becker, *J. Appl. Phys.*, 2000, **88**, 5884–5893.
18 A. Bloesser, H. Kurz, J. Timm, F. Wittkamp, C. Simon, S. Hayama, B. Weber, U. P. Apfel and R. Marschall, *ACS Appl. Nano Mater.*, 2020, **3**, 11587–11599.
19 T. P. Sumangala, I. Pasquet, L. Presmanes, Y. Thimont, C. Bonningue, N. Venkataramani, S. Prasad, V. Baco-Carles, P. Tailhades and A. Barnabé, *Ceram. Int.*, 2018, **44**, 18578–18584.
20 N. K. Thanh, T. T. Loan, N. P. Duong, L. N. Anh, D. T. T. Nguyet, N. H. Nam, S. Soontaranon, W. Klysubun and T. D. Hien, *Phys. Status Solidi A*, 2018, **215**, 1700397.
21 A. Franco, T. E. Pereira Alves, E. C. De Oliveira Lima, E. Da Silva Nunes and V. Zapf, *Appl. Phys. A: Mater. Sci. Process.*, 2009, **94**, 131–137.
22 M. G. Ferreira Da Silva and M. A. Valente, *Mater. Chem. Phys.*, 2012, **132**, 264–272.
23 R. Waldron, *Phys. Rev.*, 1955, **99**, 1727.
24 W. White and B. DeAngelis, *Spectrochim. Acta, Part A*, 1967, **23**, 985–995.
25 T. K. Pathak, N. H. Vasoya, V. K. Lakhani and K. B. Modi, *Ceram. Int.*, 2010, **36**, 275–281.
26 E. Katsnelson, A. Karoza, L. Meleshchenko, V. Pankov and B. Khavkin, *Phys. Status Solidi B*, 1987, **141**, 599–609.
27 F. Naaz, H. K. Dubey, C. Kumari and P. Lahiri, *SN Appl. Sci.*, 2020, **2**, 808.
28 P. Prajapat, S. Dhaka and H. S. Mund, *J. Electron. Mater.*, 2021, **50**, 4671–4677.
29 F. Nakagomi, S. W. da Silva, V. K. Garg, A. C. Oliveira, P. C. Morais and A. Franco, *J. Solid State Chem.*, 2009, **182**, 2423–2429.
30 H. H. Kora, M. Taha, A. A. Farghali and S. I. El-Dek, *Metall. Mater. Trans. A*, 2020, **51**, 5432–5443.
31 R. Dom, R. Subasri, K. Radha and P. H. Borse, *Solid State Commun.*, 2011, **151**, 470–473.
32 T. S. Almutairi, *ACS Omega*, 2023, **8**, 36999–37010.
33 L. I. Granone, A. C. Ulpe, L. Robben, S. Klimke, M. Jahns, F. Renz, T. M. Gesing, T. Bredow, R. Dillert and D. W. Bahnemann, *Phys. Chem. Chem. Phys.*, 2018, **20**, 28267–28278.
34 R. Dovesi, R. Orlando, A. Erba, C. M. Zicovich-Wilson, B. Civalleri, S. Casassa, L. Maschio, M. Ferrabone, M. De La Pierre, P. d'Arco, *et al.*, *Int. J. Quantum Chem.*, 2014, **114**, 1287–1317.
35 A. D. Becke, *J. Chem. Phys.*, 1992, **3**, 2155–2160.
36 C. Adamo and V. Barone, *Chem. Phys. Lett.*, 1998, **298**, 113–119.
37 A. V Krukau, O. A. Vydrov, A. F. Izmaylov and G. E. Scuseria, *J. Chem. Phys.*, 2006, **125**, 224106.
38 F. S. Gentile, W. C. Mackrodt, N. L. Allan and R. Dovesi, *Phys. Chem. Chem. Phys.*, 2020, **22**, 20612–20617.
39 M. De La Pierre, R. Orlando, L. Maschio, K. Doll, P. Ugliengo and R. Dovesi, *J. Comput. Chem.*, 2011, **32**, 1775–1784.
40 M. Catti, G. Valerio and R. Dovesi, *Phys. Rev. B: Condens. Matter Mater. Phys.*, 1995, **51**, 7441–7450.
41 M. Towler, N. Allan, N. M. Harrison, V. Saunders, W. Mackrodt and E. Apra, *Phys. Rev. B: Condens. Matter Mater. Phys.*, 1994, **50**, 5041.
42 M. Catti, A. Pavese, R. Dovesi and V. R. Saunders, *Phys. Rev. B: Condens. Matter Mater. Phys.*, 1993, **47**, 9189.
43 C. M. Zicovich-Wilson, F. Pascale, C. Roetti, V. R. Saunders, R. Orlando and R. Dovesi, *J. Comput. Chem.*, 2004, **25**, 1873–1881.
44 R. D. F. Pascale, C. M. Zicovich-Wilson, F. Lopez, B. Civalleri and R. Orlando, *J. Comput. Chem.*, 2004, **25**, 888–897.
45 L. Maschio, B. Kirtman, M. Rérat, R. Orlando and R. Dovesi, *J. Chem. Phys.*, 2013, **139**, 164101.
46 L. Maschio, B. Kirtman, R. Orlando and M. Rèrat, *J. Chem. Phys.*, 2012, **137**, 204113.
47 J. Kurian and M. J. Mathew, *J. Magn. Magn. Mater.*, 2018, **451**, 121–130.
48 S. K. Pradhan, S. Bid, M. Gateshki and V. Petkov, *Mater. Chem. Phys.*, 2005, **93**, 224–230.
49 A. Franco and M. Silva, *J. Appl. Phys.*, 2011, **109**, 07B505.
50 K. Kirchberg, A. Becker, A. Bloesser, T. Weller, J. Timm, C. Suchomski and R. Marschall, *J. Phys. Chem. C*, 2017, **121**, 27126–27138.

51 R. Köferstein, T. Walther, H. Dietrich and S. G. Ebbinghaus, *J. Mater. Sci.*, 2013, **48**, 6509–6518.
52 C. E. Rodríguez Torres, G. A. Pasquevich, P. M. Zélis, F. Golmar, S. P. Heluani, S. K. Nayak, W. A. Adeagbo, W. Hergert, M. Hoffmann, A. Ernst, P. Esquinazi and S. J. Stewart, *Phys. Rev. B: Condens. Matter Mater. Phys.*, 2014, **89**, 104411.
53 Z. K. Heiba and M. B. Mohamed, *J. Mater. Sci.: Mater. Electron.*, 2019, **30**, 786–796.
54 D. Narsimulu, B. N. Rao, M. Venkateswarlu, E. S. Srinadhu and N. Satyanarayana, *Ceram. Int.*, 2016, **42**, 16789–16797.
55 Z. Wang, P. Lazor, S. Saxena and H. C. St O, *Mater. Res. Bull.*, 2002, **37**, 1589–1602.